

Fourier Fingerprints of Ansatzes in Quantum Machine Learning

Melvin Strobl ^{1*}, M. Emre Sahin ², Lucas van der Horst ¹,
Eileen Kuehn ¹, Achim Streit ¹, and Ben Jaderberg ³

^{1*}Karlsruhe Institute of Technology, 76344 Eggenstein-Leopoldshafen, Germany.

²The Hartree Centre, STFC,
Sci-Tech Daresbury, Warrington, WA4 4AD, United Kingdom.

³IBM Quantum, IBM Research Europe,
Hursley, Winchester, SO21 2JN, United Kingdom.

*Corresponding author(s). E-mail(s): melvin.strobl@kit.edu;

Abstract

Typical schemes to encode classical data in variational quantum machine learning (QML) lead to quantum Fourier models with $\mathcal{O}(\exp(n))$ Fourier basis functions in the number of qubits. Despite this, in order for the model to be efficiently trainable, the number of parameters must scale as $\mathcal{O}(\text{poly}(n))$. This imbalance implies the existence of correlations between the Fourier modes, which depend on the structure of the circuit. In this work, we demonstrate that this phenomenon exists and show cases where these correlations can be used to predict ansatz performance. For several popular ansatzes, we numerically compute the Fourier coefficient correlations (FCCs) and construct the *Fourier fingerprint*, a visual representation of the correlation structure. We subsequently show how, for the problem of learning random Fourier series, the FCC correctly predicts relative performance of ansatzes whilst the widely-used expressibility metric does not. Finally, we demonstrate how our framework applies to the more challenging problem of jet reconstruction in high-energy physics. Overall, our results demonstrate how the Fourier fingerprint is a powerful new tool in the problem of optimal ansatz choice for QML.

Keywords: Quantum Computing, Quantum Machine Learning, Quantum Fourier Models, Ansatz Selection, High-Energy Physics

1 Introduction

The field of quantum machine learning (QML) has emerged as one of the most rapidly advancing areas of quantum computing in recent years [4]. In particular, QML has seen a significant focus on the use of parameterized quantum circuits (PQCs) as machine learning models [1, 21]. Here, in a way that is conceptually similar to deep neural networks, the parameters of a quantum circuit are trained to learn the function $f(\mathbf{x}, \boldsymbol{\theta})$ that best approximates a given dataset of input-output pairs $(\mathbf{x}, f(\mathbf{x}, \boldsymbol{\theta}))$. Due to its applicability to a wide range of domains [13, 19, 22, 14] and amenability to running on pre-fault-tolerant quantum computers [24, 5], PQCs remain one of the most widely-used paradigms in QML.

In this framework, a typical QML model consists of quantum feature maps (FMs) $\hat{U}_F(\mathbf{x})$, which encode a classical input \mathbf{x} into the Hilbert space, and variational ansatzes $\hat{U}_A(\boldsymbol{\theta})$ which manipulate the input via trainable parameterized gates $\boldsymbol{\theta}$. Importantly, the output of these models can be represented as a partial Fourier series in the input [28], giving rise to the name quantum Fourier models (QFMs). Fully understanding how the choice of feature map and ansatz affects the Fourier spectrum of QFMs, both analytically [36] and numerically [15, 20, 7], remains crucial for maximizing performance and probing dequantization [34].

In this work, we demonstrate a novel phenomenon in which correlations naturally arise between the coefficients of the Fourier series of efficiently-trainable QFMs. This implies that QFMs are not able to control each term in their Fourier series independently, limiting the space of functions that can be practically learned. We first theoretically motivate this in Sec. 2.1 and subsequently numerically validate the existence of these correlations for a range of popular ansatzes in Sec. 2.2. Furthermore, we find the specific correlation pattern to be unique for each ansatz, which we thus call the *Fourier fingerprint* of the model. An overview of this concept is pictured in Fig. 1.

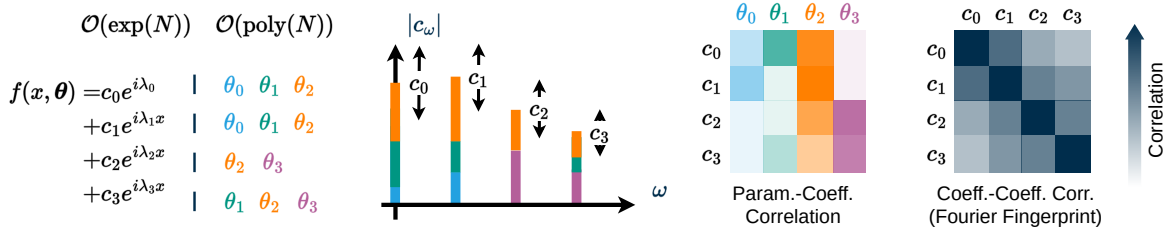


Fig. 1: The output $f(x, \boldsymbol{\theta})$ of an n qubit QFM is a truncated Fourier series with $\mathcal{O}(\exp(n))$ terms. To be efficiently trainable, this can only be tuned by $\mathcal{O}(\text{poly}(n))$ parameters. This leads to a subset of the Fourier coefficients depending on the same parameters, inducing an effective correlation between them. Practically, this implies that QFMs cannot independently control each frequency.

Subsequently, we demonstrate in practice how the *Fourier coefficient correlation (FCC)*, the average of the fingerprint, can be used to identify the best-performing ansatzes in Sec. 3.1. We find that, for learning random 1D Fourier series, models with lower FCC perform better, even in cases where expressibility would predict the ansatz to be worse. Furthermore, we extend our experiments to learning 2D Fourier series, where we observe the same result.

Finally, in Sec. 3.2, we show how the FCC can be used to pick well-performing ansatzes in the more challenging problem of 2D jet reconstruction in high-energy physics. Given the energy and momentum of a two-particle collision, we train our model to predict the transverse momentum of the largest jet.

Comparing the performance of different ansatzes, we find a similar trend as observed in the experiments concerning random Fourier series, *i.e.* that models with lower average FCC achieve lower mean squared error (MSE). Overall, our results highlight that the Fourier fingerprint and the resultant FCC metric are practically useful and should be integrated into the process of ansatz choice in QML.

2 Method

2.1 Correlation between coefficients in quantum Fourier models

Let us define an L -layer QFM by $U(\mathbf{x}, \boldsymbol{\theta}) = W^{(L+1)}(\boldsymbol{\theta})S(\mathbf{x})W^{(L)} \dots W^{(2)}S(\mathbf{x})W^{(1)}$, with trainable unitaries W and n -qubit encoding gates S taking a D dimensional input \mathbf{x} . For this class of models, which includes quantum neural networks (QNNs), the output $f(\mathbf{x}, \boldsymbol{\theta}) = \langle 0|^{\otimes n} U^\dagger(\mathbf{x}, \boldsymbol{\theta}) \mathcal{M} U(\mathbf{x}, \boldsymbol{\theta}) |0\rangle^{\otimes n}$ is obtained by measuring an expectation value of an observable \mathcal{M} . The seminal work of Ref. [28] showed the equivalence of this expression to a truncated Fourier series

$$f(\mathbf{x}, \boldsymbol{\theta}) = \sum_{\boldsymbol{\omega} \in \boldsymbol{\Omega}} c_{\boldsymbol{\omega}}(\boldsymbol{\theta}) \exp(i\boldsymbol{\omega}\mathbf{x}) \quad (1)$$

where $\boldsymbol{\Omega}$ defines the set of frequencies and $c_{\boldsymbol{\omega}}$ the complex valued coefficient belonging to the frequency vector $\boldsymbol{\omega}$.

From Eq. 1, we first note that the Fourier coefficients of the model are explicitly dependent on the trainable parameters $\boldsymbol{\theta} \in \Theta$ of the ansatz¹. The frequency spectrum of this QFM, and specifically models where the output is an expectation value, is defined by the gaps in the eigenspectrum of the FM generator Hamiltonian [28, 20]

$$f(\mathbf{x}, \boldsymbol{\theta}) = \sum_{i=1}^D \sum_{\mathbf{j}, \mathbf{k} \in \llbracket 1, d_l \rrbracket_{l=1}^L} c_{\mathbf{j}, \mathbf{k}}(\boldsymbol{\theta}) \exp(i(\Lambda_{i, \mathbf{j}} - \Lambda_{i, \mathbf{k}}) \mathbf{e}_i^T \mathbf{x}) \quad | \quad \mathbf{j}, \mathbf{k} \in \llbracket 1, d_l \rrbracket_{l=1}^L, \quad (2)$$

where $\llbracket \cdot \rrbracket$ defines the product of the intervals $j_l, k_l \in [1, d_l]$ in the multi-index \mathbf{j}, \mathbf{k} and $\Lambda_{i, \mathbf{j}} = \lambda_{j_1}^i + \lambda_{j_2}^i + \dots + \lambda_{j_L}^i$ is the sum of all d_l eigenvalues of the l -th generator in L layers for input index i . Whilst typically $\boldsymbol{\Omega}$ is defined as the *unique* gaps in the spectrum, here it is useful to define a larger set of frequencies that includes degenerate values

$$\tilde{\boldsymbol{\Omega}} = \biguplus_{i=1}^D \{\Lambda_{i, \mathbf{j}} - \Lambda_{i, \mathbf{k}}\} \quad | \quad \mathbf{j}, \mathbf{k} \in \llbracket 1, d_l \rrbracket_{l=1}^L, \quad (3)$$

Importantly, whilst the scaling of unique frequencies is determined by the degeneracy of the FM eigenspectrum [27], the absolute number of terms in the Fourier series always grows as $|\tilde{\boldsymbol{\Omega}}| \sim \mathcal{O}(2^{nD})$.

Finally, we note that for QFMs to be efficiently trainable, they must contain a sub-exponential $|\boldsymbol{\theta}| \sim \mathcal{O}(\text{poly}(n))$ number of parameters, since the time complexity of training is linear in $|\boldsymbol{\theta}|$. Combining these observations about the size of $|\tilde{\boldsymbol{\Omega}}|$ and $|\boldsymbol{\theta}|$, it is immediately apparent that in the asymptotic limit there is no injective map between the set of Fourier coefficients $c_{\boldsymbol{\omega}}$ and $\boldsymbol{\theta}$. Therefore, the coefficients $c_{\boldsymbol{\omega}}(\boldsymbol{\theta})$ must depend on a *shared* set of ansatz parameters, which implies the existence of correlations between the coefficients of different terms in the Fourier series. We provide another perspective on this statement in App. E.

¹The coefficients also implicitly depend on the FM as the degeneracy of the encoding spectrum upper-bounds the variance of the coefficients [20].

The practical implication of this result is that the training of QFMs is in fact an optimization of Fourier series where each term is not independent. This is an additional constraint, which is not apparent from the form of Eq. 1, that reduces the possible solution space. Furthermore, this is in contrast to classical approaches to Fourier regression, where modes are tuned independently [3, 11]. In Sec. 3 we numerically show how this constraint for QFMs affects performance, whilst in App. G we analytically consider how this constraint appears in the MSE loss.

2.2 Computing the Fourier fingerprint

Given a QFM, we numerically compute the correlations between Fourier coefficients as follows. For a randomly initialized set of ansatz parameters θ , we evaluate $f(\mathbf{x}, \theta)$ for many different $\mathbf{x} \in \mathcal{X}$ such that the number of samples satisfies the Shannon-Nyquist [30] criterion. We then obtain the Fourier coefficients \mathbf{c} using the fast Fourier transform (FFT), specifically as implemented in the QML-Essentials framework [33]. As the FFT requires knowledge of the number of frequencies in advance, in the remainder of this work we consider a single-qubit Pauli encoding, such that $\Omega = \llbracket -nL, nL \rrbracket^D$, based on Eq. 3 under the assumption $d_l = 2 \forall l \in [1 \dots L]$.

We then repeat this procedure M times for randomly sampled ansatz parameters θ from the space of possible ansatz parameters Θ , obtaining a set of M Fourier coefficient vectors. Specifically, each $\theta \in \Theta$ is i.i.d. and drawn from a uniform distribution with the interval $[0, 2\pi]$. Treating each calculated instance of \mathbf{c} as independent samples, we then compute the Pearson correlation coefficient [9]

$$r_{\Theta}(\omega, \omega') = \frac{\sum_{\theta \in \Theta} (c_{\omega}(\theta) - \bar{c}_{\omega})(c_{\omega'}(\theta) - \bar{c}_{\omega'})}{\sqrt{\sum_{\theta \in \Theta} (c_{\omega}(\theta) - \bar{c}_{\omega})^2 \sum_{\theta \in \Theta} (c_{\omega'}(\theta) - \bar{c}_{\omega'})^2}} \quad (4)$$

between each possible pair in the spectrum. Here, \bar{c}_{ω} and $\bar{c}_{\omega'}$ represent the average value of the coefficient at frequency ω and ω' respectively. Note that the Pearson correlation is normalized by the standard deviation of the coefficients at each frequency. We provide a sanity check of this in Fig. 8 where we randomly sample coefficients with an increasing number of redundancies towards higher frequencies. Computing the correlation between them results in zeros for all frequency pairs, which confirms that the variance is mitigated, meaning that the decaying variance towards higher frequencies as observed in [20] is taken into account with the FCC metric.

We compute this correlation specifically for an $n = 6$, $L = 1$ QFM with the 1D feature map $S = \bigotimes^n R_Y^{(n)}(x)$ and observable $\mathcal{M} = \frac{1}{n} \sum_i^n \sigma_i^z$. Fig. 2a shows a visualization of the computed correlations for a range of ansatzes. It can be observed, that *e.g.* the hardware-efficient ansatz (HEA) results in a QFM with significantly larger correlations between high-frequency indices whereas *Circuit 15* has a minimal correlation across all coefficients. Generally, the distribution of correlations differs significantly between the ansatzes, prompting us to coin the term *Fourier fingerprint* to describe this unique distribution for each ansatz. Note that the axes are shifted by one coefficient index as we only show the lower triangle of the correlation matrix, *i.e.* the unique correlation without the trivial diagonal.

Furthermore, the concept of correlations between Fourier coefficients can be extended to higher input dimensions D as stated in Eq. 3. Here, ω becomes a vector of frequencies and each coefficient is indexed by $c_{(\omega_0, \omega_1)}$ for the case of $d = 2$. The correlation is then computed, similar to the 1D case, but taking into account each possible combination of frequencies, resulting in Fig. 2b where we visualize the fingerprint of a single ansatz for a 2D model, with feature map $S = \bigotimes^n R_X^{(n)}(x_1) \bigotimes^n R_Y^{(n)}(x_2)$. In this work, we use $500 \cdot |\theta| \cdot 2^n \cdot D$ samples to compute the correlations to high accuracy. However, we stress that to measure the correlation to a fixed error, the number of samples does not need to grow exponentially with n as shown in App. J.

Based on these fingerprints, we introduce the *Fourier coefficient correlation (FCC)* in Eq. 5 as a metric that quantifies the average correlation between the coefficients.

$$\text{FCC}_\Theta := \frac{1}{|\Omega|} \sum_{\omega, \omega' \in \Omega} |r_\Theta(\omega, \omega')|. \quad (5)$$

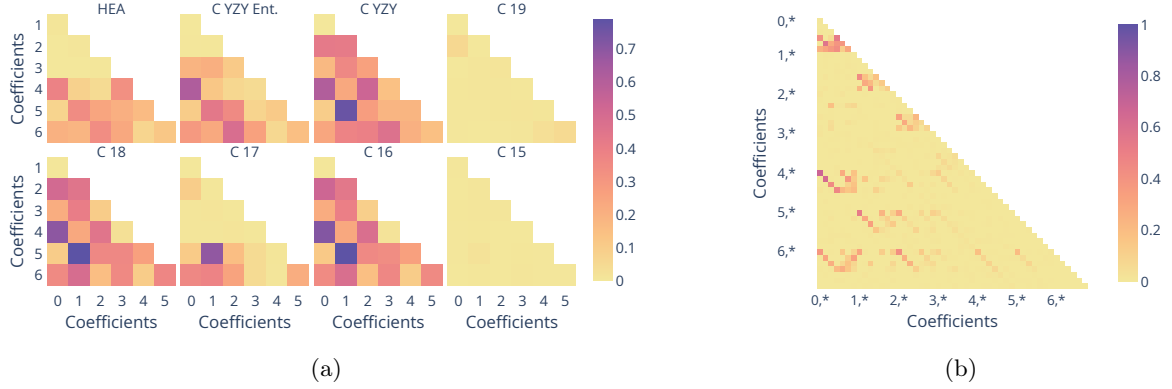


Fig. 2: Fourier fingerprints visualizing the correlation between different Fourier coefficients (index as tick labels) of QFMs. Circuits with the name C_* are from Ref. [32], whilst the rest of the ansatzes are defined in App. A. (a) Comparison between several different ansatzes for a 1D model. (b) Fingerprint of a 2D model for the HEA only. Here, the index reads $c_{i,*} = \{c_{i,0} \dots c_{i,6}\}$.

3 Results

3.1 Learning random Fourier series

To investigate the predictive power of the FCC metric for ansatz performance, we train a model on a truncated Fourier series \hat{f} such that it minimizes the MSE loss

$$\mathcal{L}_{\text{MSE}} = \frac{1}{|\mathcal{X}|} \int_{\mathbf{x} \in \mathcal{X}} |f(\mathbf{x}, \boldsymbol{\theta}) - \hat{f}(\mathbf{x})|^2 d\mathbf{x}, \quad (6)$$

where the data comes from the family of random Fourier series

$$\hat{f}(\mathbf{x}) = \sum_{\omega \in \hat{\Omega}} \hat{c}_\omega \exp(i\omega \mathbf{x}). \quad (7)$$

Here, \hat{c}_ω are uniformly drawn complex numbers within the unit circle, *i.e.* $\sqrt{r}e^{-i2\pi p}$ with $r, p \in \mathcal{U}(0, 1]$, satisfying $|\hat{c}_\omega| \leq 1$. The frequencies of the dataset $\hat{\Omega}$ are explicitly set to the same frequencies as those generated by the FM of the QFM models Ω . This ensures that the target function is within the learnable domain of the QFMs assuming perfectly independent coefficients. Furthermore, the inputs \mathbf{x} are sampled according to the Nyquist-Shannon sampling theorem [30], *i.e.* $|\mathcal{X}| = 2 \max(\Omega)$ in the interval $[0, 2\pi)$.

We evaluate the MSE across multiple randomly seeded models and Fourier coefficients and average over the results to derive a performance index. Specifically, we use 10 different model initialization and 10 different dataset seeds, yielding a total of 100 runs per ansatz. We compute the expressibility using the QML-Essentials package [33], with $500 \cdot |\boldsymbol{\theta}| \cdot 2^n$ parameter samples and 75 histogram bins.

In [App. H](#) we provide details on the computation of the expressibility and a comparison to the FCC in terms of complexity. Here we find that computing the FCC incurs a lower overhead both on classical and quantum hardware, making it a more scalable metric for comparing ansatzes.

The results for the 1D case are visualized in [Fig. 3a](#). Here, the FCC and expressibility are represented by different colors, whereas each symbol indicates a different QML ansatz. In line with the observations from [Fig. 2a](#), *Circuit 19* shows a similar FCC value to *Circuit 15*, but the resulting MSE is slightly higher. For *Circuit YZY* and *Circuit 18*, the MSEs are almost identical, while the FCCs deviate slightly. Following this, we observe that, overall, the FCC correlates almost linearly with the MSE, with the lowest and highest values of the FCC being 4.57×10^{-3} (*Circuit 15*) and 0.323 (*Circuit 18*), respectively. The expressibility, in contrast, does not allow for a conclusive statement and fails to correctly predict the order of the final MSE for every ansatz.

Employing a second Pauli encoding gate, orthogonal to the first, we replicate this training on a two-dimensional Fourier series, subsequently calculating the FCC. The Fourier series dataset is then naturally extended to a two-dimensional dataset, yielding the results shown in [Fig. 3b](#).

Here, one can see that *Circuit 15* is now an outlier in the otherwise almost linear relationship between MSE and FCC. This outlier can be explained by the fact that *Circuit 15* lacks the imaginary part of the coefficients when being joint by a Pauli-RX feature map, which we used to encode the second input dimension (*c.f.* [App. C](#)). The absence of an imaginary part depending on the rotational axis was also shown in [\[8\]](#) for this specific circuit and is included in [App. C](#).

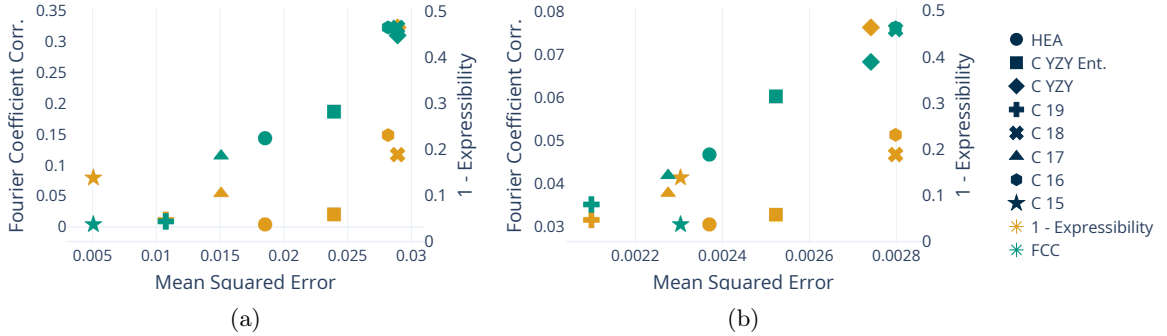


Fig. 3: Comparison between the [FCC](#) and [expressibility complement](#) of models with different ansatzes versus the averaged mean squared error (MSE) when fitting Fourier series. Here, each model is trained from 10 random initializations and evaluated against 10 different (a) 1D and (b) 2D Fourier series with random coefficients.

Overall, the results on the 1D and 2D Fourier series reveal a clear relationship between the MSE and the FCC, indicating that this metric provides a more powerful tool for predicting model performance in these cases. Importantly, in both sets of experiments, the widely-used expressibility metric incorrectly identifies which ansatzes would perform the best. We note that the standard deviations are significantly smaller than the plotted values for all measures and are mostly consistent across all ansatzes (*c.f.* [App. F](#)).

3.2 Application to High-Energy Physics

High-energy physics (HEP) is a widely studied application and benchmark for QML [\[29, 35, 10\]](#). In this section, we apply the same methodology from [Sec. 3.1](#) to the more challenging HEP problem of 2D jet reconstruction.

Specifically, we train a QFM to reconstruct the highest transverse momentum p_T (*i.e.* the transverse momentum of the leading jet) using the four-vector (E, p_x, p_y, p_z) of two colliding particles. In each of the synthetically generated collision events, two protons collide along the z -axis, where their constituent partons interact and produce, through a series of further interactions, decays and final hadronization, sprays of particles observed by the detector as a cluster of hadron jets. Since the partons travel exclusively along z and the LHC detector is symmetric about this axis, only the transverse momenta components in the x and y directions are relevant. In the following numerical experiments, we utilize the dataset published in Ref. [12].

In contrast to Sec. 3.1, our assumption that the frequencies of the dataset match those of the QFM can't be guaranteed in this case, making this problem potentially harder for the model to learn. We first analyze the dataset to identify a subset of the most relevant input features for prediction. We find that the type of particle and charge have negligible influence on the leading p_T , which aligns with physical expectations. Meanwhile, we identify two input features that can be computed from the data that have a large effect on the leading p_T , the center-of-mass energy $E_{\text{CM}} = \sqrt{(E^{(1)} + E^{(2)})^2 - (p_z^{(1)} + p_z^{(2)})^2}$ and the absolute energy difference $E_{\Delta} = |E^{(1)} - E^{(2)}|$. Note that due to the aforementioned symmetry, $p_x = p_y = 0$. On these features, we apply a uniform quantile transformer to E_{CM} and E_{Δ} resulting in a uniform distribution of the input features in the interval $[0, 2\pi)$. We then discretize this distribution to ensure equally spaced input features as conceptually visualized in Fig. 4.

We first benchmark the complexity of this problem by applying a classical machine learning (ML) model. We train a classical multi-layer perceptron (MLP) consisting of 2 hidden layers and 8 neurons per layer, resulting in 105 trainable parameters, on the supervised learning task of predicting p_T from the input features. While being small in size, the number of parameters of this classical model still exceeds those of the QFM tested in this work. We train the classical model with a batch size of 256 on a combination of the Kullback-Leibler (KL) divergence (KLDiv) and the Huber loss as $\mathcal{L} = \text{KLDiv} + 0.001 \cdot \text{HuberLoss}$ using the Adam optimizer [16] with a learning rate of 0.05, adjusted dynamically via a learning rate scheduler. We justify the choice of this loss function as we aim to learn the momenta distribution of the dataset, due to the probabilistic nature of the task and no one-to-one input to output mapping, which KLDiv naturally models. Input features are scaled using “MinMax” scaling, while the leading p_T is left unscaled. KL-divergence is used exclusively for validation and testing, while we add a small Huber loss during training, as it empirically improved convergence stability.

Training is performed on 200 000 events with a ratio of 80% for training, 10% for validation and 10% for testing. On average, across 10 random models, the classical MLP obtained a KL divergence score of 0.163 ± 0.049 . However, selecting the 10 best-performing models from a pool of 30 improved the result significantly, yielding a KL divergence of 0.035 ± 0.005 . Despite trying multiple engineering tactics - including varying model architecture, model size, and learning strategies - performance did not improve. Consequently, we selected the simplest solution that still yielded competitive results.

Following an evaluation of the classical model, we shift our attention to the QFM. As in previous experiments described in Sec. 3.1, we use 10 different model initializations and 10 different dataset initializations. In contrast to the preliminary experiments on MLP, we reduce the dataset size to 40 000 with a ratio of 80% for training, 10% for validation and 10% for testing, both for any subsequent experiments on the MLP and QFM. We switch the previous “MinMax” scaler of the classical MLP to a “uniform quantile transformer” as in the QFM. Similarly, the target values using “MinMax” scaling and compared with the predicted values combining the MSE and KL-divergence loss [17] $\mathcal{L} = \text{MSE} + 0.001 \cdot \text{KLDiv}$ yields the best results in conjunction with an Adam optimizer [16] with a learning rate of 0.005.

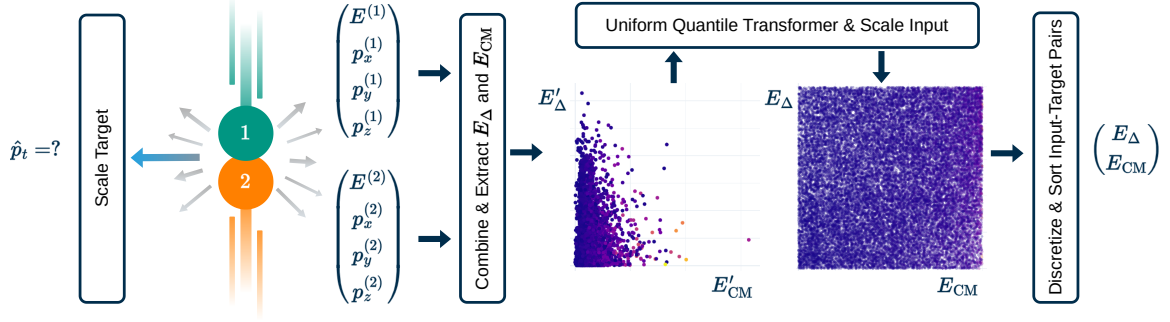


Fig. 4: Problem definition and data mapping for the HEP dataset. The colliding particles (1) and (2) are characterized by the four vector (E, p_x, p_y, p_z) , which are then transformed into the center-of-mass energy E_{CM} and the energy difference $E_{\Delta} = |E^{(1)} - E^{(2)}|$. Afterwards a “uniform quantile transformer” is applied to the features, which are then discretized and used to predict the scaled transverse momentum p_T of the leading jet.

A comparison between the results obtained by the MLP and QFM is shown in Fig. 5a. Specifically, we plot the distribution of absolute differences between the predicted and true p_T values in each case. Here, we observe that both models achieve a low mean deviation of 0.382 and 0.050 for the MLP and QFM, respectively. However, the standard deviation of the absolute differences is lower for the QFM with a standard deviation of 3.61 compared to 6.13 for the MLP. Overall, our results validate that the problem is non-trivial to solve with a standard MLP, and that our trained QFM produces a competitive benchmark.

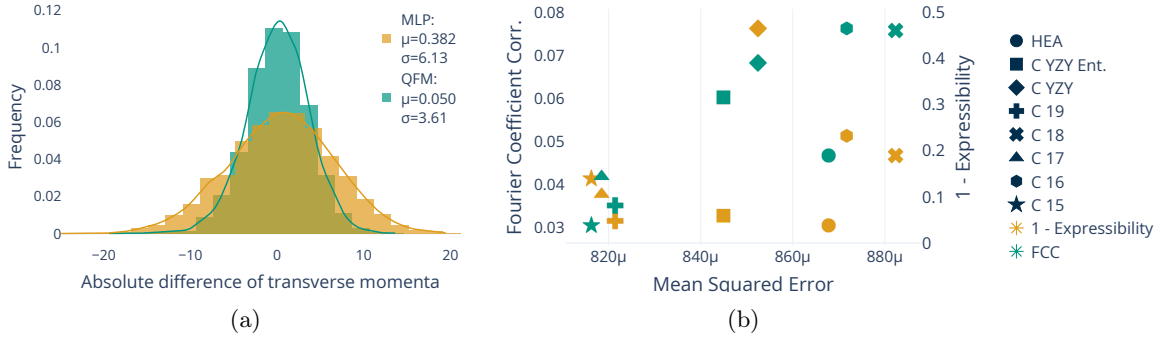


Fig. 5: Training performance (validation score) of (a): the MLP and QFM visualized as distributions of the differences between the target p_T and the ground truth and (b): Training performance (validation score) of the model on the HEP dataset. Averaged over 10 independent dataset seeds and 10 distinct parameter initializations.

In Fig. 5b we show the comparison of the predicted performance of the FCC and expressibility for the HEP dataset. When observing the FCC, *Circuit 17* and the “Hardware Efficient Ansatz” can be identified as outliers. The ansatz with the lowest and highest FCC, *Circuit 15* and *Circuit 18*, correlate to the lowest and highest MSE, respectively. Although the order of MSEs is not perfectly predicted by the FCCs here, we observe a clear overall trend linking correlation and performance. Compared to expressibility, both metrics successfully predict the same clusters of ansatzes while the FCC is computationally less expensive as discussed in App. H. In addition to the results considering the MSE, we provide the results for the KL divergence and Huber loss in App. I.

4 Conclusion & discussion

In this work, we have demonstrated the existence of correlations between the Fourier coefficients of QFMs and its impact on performance for several popular ansatzes. In [Sec. 2](#), we introduced the theoretical motivation as to why these correlations exist and how they can be numerically calculated by repeatedly sampling random instances of the model. In [Sec. 3.1](#), we showed how, for the task of learning random Fourier series, models with lower average FCC consistently perform better for both 1D and 2D inputs. Finally, in [Sec. 3.2](#) we evidenced how this relationship extends to problems of practical interest such as the more challenging setting of 2D jet reconstruction in high-energy physics.

Despite our numerical results, we note that correlations between the Fourier coefficients of efficiently-trainable QFMs are only asymptotically guaranteed for feature maps that produce exponentially many *unique* frequencies. This includes the Goulomb encoding [\[25\]](#) as well as those in Refs. [\[31, 18\]](#). Whilst the feature maps used in this work produce QFMs with exponentially many basis functions, in contrast, there are only a linear number of unique modes due to degeneracy in the eigenspectrum. This implies that it may be possible to design an ansatz that, in combination with a degenerate feature map, could have fully independent Fourier coefficients. This could be achieved by ensuring each parameter only appears in the coefficients of terms with the same frequency. Nevertheless, our results highlight that this phenomenon does not occur in popular ansatzes. Understanding what such an ansatz would look like, and if it is efficiently implementable, remains an interesting open question.

Following this, the aspect of trainability should also be considered an important area of future research. Ragone et al. [\[26\]](#) showed that ansatzes with high expressibility are very unlikely to be trainable, raising the interesting question of whether a similar pattern translates to the FCC. The numerical results presented in this paper do not strictly imply that a high expressibility correlates with a low FCC (*c.f.* [Fig. 3](#)), suggesting a non-trivial relationship between these metrics. Therefore, it cannot be ruled out that a lower FCC, *i.e.* ansatzes with highly-independent coefficients, are generally not trainable.

Finally, in this work, we studied only one instance of a real-world dataset. As a future direction of research, it remains to be seen whether the same trends hold for other problems, whereby ansatzes with the lowest average FCC perform the best. In particular, this heuristic has the underlying assumption that the frequencies of the dataset are themselves independent. If this is not true, one may find that the best QML model is one which purposefully produces Fourier coefficients with large correlations specifically tied to the data. In this way, the FCC may be better thought of as an inductive bias to encode into QFMs, instead of as a metric to always minimize.

Acknowledgements

We thank Gabriel Mejía Ruiz for helpful discussions on mathematical formulations and Maja Franz for valuable discussions concerning QFMs in a broader view.

We want to express our gratitude to Ryan Sweke and Christa Zoufal for their useful discussions and insights.

MS, EK and AS acknowledge support by the state of Baden-Württemberg through bwHPC.

This work was supported by the Hartree National Centre for Digital Innovation, a collaboration between the Science and Technology Facilities Council and IBM.

References

- [1] Marcello Benedetti, Erika Lloyd, Stefan Sack, et al. “Parameterized quantum circuits as machine learning models”. In: *Quantum science and technology* 4.4 (2019), p. 043001.
- [2] A. L. Bowley. “The Standard Deviation of the Correlation Coefficient”. In: *Journal of the American Statistical Association* 23.161 (1928), pp. 31–34. DOI: [10.1080/01621459.1928.10502991](https://doi.org/10.1080/01621459.1928.10502991).
- [3] Evan B Brooks, Valerie A Thomas, Randolph H Wynne, et al. “Fitting the multitemporal curve: A Fourier series approach to the missing data problem in remote sensing analysis”. In: *IEEE Transactions on Geoscience and Remote Sensing* 50.9 (2012), pp. 3340–3353.
- [4] Marco Cerezo, Guillaume Verdon, Hsin-Yuan Huang, et al. “Challenges and opportunities in quantum machine learning”. In: *Nature computational science* 2.9 (2022), pp. 567–576.
- [5] Jiachen Chen, Yaozu Wu, Zhen Yang, et al. “Quantum ensemble learning with a programmable superconducting processor”. In: *npj Quantum Information* 11.1 (2025), p. 83.
- [6] James W. Cooley and John W. Tukey. “An Algorithm for the Machine Calculation of Complex Fourier Series”. In: *Mathematics of Computation* 19.90 (1965), pp. 297–301. DOI: [10.1090/S0025-5718-1965-0178586-1](https://doi.org/10.1090/S0025-5718-1965-0178586-1).
- [7] Callum Duffy and Marcin Jastrzebski. “Spectral Bias in Variational Quantum Machine Learning”. In: *arXiv preprint arXiv:2506.22555* (2025).
- [8] Maja Franz, Melvin Strobl, Leonid Chaichenets, et al. *Out of Tune: Demystifying Noise-Effects on Quantum Fourier Models*. 2025. DOI: [10.48550/arxiv.2506.09527](https://doi.org/10.48550/arxiv.2506.09527).
- [9] David Freedman, Robert Pisani, and Roger Purves. “Statistics (international student edition)”. In: *Pisani, R. Purves, 4th edn. WW Norton & Company, New York* (2007).
- [10] Wen Guan, Gabriel Perdue, Arthur Pesah, et al. “Quantum machine learning in high energy physics”. en. In: *Machine Learning: Science and Technology* 2.1 (2021). Publisher: IOP Publishing, p. 011003. DOI: [10.1088/2632-2153/abc17d](https://doi.org/10.1088/2632-2153/abc17d).
- [11] Venkatesan Guruswami and David Zuckerman. “Robust Fourier and polynomial curve fitting”. In: *2016 IEEE 57th Annual Symposium on Foundations of Computer Science (FOCS)*. IEEE. 2016, pp. 751–759.
- [12] Yacine Haddad and Michele Grossi. *Parton-to-Jet Mapping proton-proton dataset at 14 TeV*. Zenodo, June 2025. DOI: [10.5281/zenodo.15689696](https://doi.org/10.5281/zenodo.15689696).
- [13] Vojtěch Havlíček, Antonio D Córcoles, Kristan Temme, et al. “Supervised learning with quantum-enhanced feature spaces”. In: *Nature* 567.7747 (2019), pp. 209–212.
- [14] Ben Jaderberg, Antonio A Gentile, Atiyo Ghosh, et al. “Potential of quantum scientific machine learning applied to weather modeling”. In: *Physical Review A* 110.5 (2024), p. 052423.
- [15] Ben Jaderberg, Antonio A. Gentile, Youssef Achari Berrada, et al. *Let Quantum Neural Networks Choose Their Own Frequencies*. Tech. rep. arXiv, Sept. 2023. DOI: [10.48550/arXiv.2309.03279](https://doi.org/10.48550/arXiv.2309.03279).
- [16] Diederik P. Kingma and Jimmy Ba. *Adam: A Method for Stochastic Optimization*. 2017. DOI: [10.48550/arXiv.1412.6980](https://doi.org/10.48550/arXiv.1412.6980).
- [17] S. Kullback and R. A. Leibler. “On Information and Sufficiency”. In: *The Annals of Mathematical Statistics* 22.1 (Mar. 1951). Publisher: Institute of Mathematical Statistics, pp. 79–86. DOI: [10.1214/aoms/1177729694](https://doi.org/10.1214/aoms/1177729694).
- [18] Oleksandr Kyriienko, Annie E Paine, and Vincent E Elfving. “Protocols for trainable and differentiable quantum generative modeling”. In: *Physical Review Research* 6.3 (2024), p. 033291.
- [19] Seth Lloyd, Maria Schuld, Aroosa Ijaz, et al. “Quantum embeddings for machine learning”. In: *arXiv preprint arXiv:2001.03622* (2020).
- [20] Hela Mhiri, Leo Monbroussou, Mario Herrero-Gonzalez, et al. *Constrained and Vanishing Expressivity of Quantum Fourier Models*. Mar. 2024. DOI: [10.48550/arXiv.2403.09417](https://doi.org/10.48550/arXiv.2403.09417).
- [21] Kosuke Mitarai, Makoto Negoro, Masahiro Kitagawa, et al. “Quantum circuit learning”. In: *Physical Review A* 98.3 (2018), p. 032309.
- [22] Lento Nagano, Alexander Miessen, Tamiya Onodera, et al. “Quantum data learning for quantum simulations in high-energy physics”. In: *Physical Review Research* 5.4 (2023), p. 043250.

- [23] Nikita A. Nemkov, Evgeniy O. Kiktenko, and Aleksey K. Fedorov. “Fourier expansion in variational quantum algorithms”. In: *Physical Review A* 108.3 (Sept. 2023), p. 032406. DOI: [10.1103/PhysRevA.108.032406](https://doi.org/10.1103/PhysRevA.108.032406).
- [24] Xiaoxuan Pan, Xi Cao, Weiting Wang, et al. “Experimental quantum end-to-end learning on a superconducting processor”. In: *npj Quantum Information* 9.1 (2023), p. 18.
- [25] Evan Peters and Maria Schuld. *Generalization despite overfitting in quantum machine learning models*. Tech. rep. arXiv, Sept. 2022. DOI: [10.48550/arXiv.2209.05523](https://doi.org/10.48550/arXiv.2209.05523).
- [26] Michael Ragone, Bojko N. Bakalov, Frédéric Sauvage, et al. “A Lie Algebraic Theory of Barren Plateaus for Deep Parameterized Quantum Circuits”. In: *Nature Communications* 15.1 (Aug. 2024), p. 7172. DOI: [10.1038/s41467-024-49909-3](https://doi.org/10.1038/s41467-024-49909-3).
- [27] Maria Schuld, Alex Bocharov, Krysta Svore, et al. “Circuit-centric quantum classifiers”. In: *Physical Review A* 101.3 (Mar. 2020), p. 032308. DOI: [10.1103/PhysRevA.101.032308](https://doi.org/10.1103/PhysRevA.101.032308).
- [28] Maria Schuld, Ryan Sweke, and Johannes Jakob Meyer. “The effect of data encoding on the expressive power of variational quantum machine learning models”. In: *Physical Review A* 103.3 (Mar. 2021), p. 032430. DOI: [10.1103/PhysRevA.103.032430](https://doi.org/10.1103/PhysRevA.103.032430).
- [29] Tim Schwägerl, Cigdem Issever, Karl Jansen, et al. “Particle track reconstruction with noisy intermediate-scale quantum computers”. In: (2023). DOI: [10.48550/arXiv.2303.13249](https://doi.org/10.48550/arXiv.2303.13249).
- [30] C.E. Shannon. “Communication in the Presence of Noise”. In: *Proceedings of the IRE* 37.1 (1949), pp. 10–21. DOI: [10.1109/JRPROC.1949.232969](https://doi.org/10.1109/JRPROC.1949.232969).
- [31] Seongwook Shin, Yong-Siah Teo, and Hyunseok Jeong. “Exponential data encoding for quantum supervised learning”. In: *Physical Review A* 107.1 (2023), p. 012422.
- [32] Sukin Sim, Peter D. Johnson, and Alán Aspuru-Guzik. “Expressibility and Entangling Capability of Parameterized Quantum Circuits for Hybrid Quantum-Classical Algorithms”. en. In: *Advanced Quantum Technologies* 2.12 (2019), p. 1900070. DOI: [10.1002/qute.201900070](https://doi.org/10.1002/qute.201900070).
- [33] Melvin Strobl, Maja Franz, Eileen Kuehn, et al. *QML Essentials – A framework for working with Quantum Fourier Models*. 2025. DOI: [10.48550/arXiv.2506.06695](https://doi.org/10.48550/arXiv.2506.06695).
- [34] Ryan Sweke, Erik Recio-Armengol, Sofiene Jerbi, et al. “Potential and limitations of random Fourier features for dequantizing quantum machine learning”. In: *Quantum* 9 (Feb. 2025), p. 1640. DOI: [10.22331/q-2025-02-20-1640](https://doi.org/10.22331/q-2025-02-20-1640).
- [35] Cenk Tüysüz, Federico Carminati, Bilge Demirköz, et al. “Particle Track Reconstruction with Quantum Algorithms”. In: *EPJ Web of Conferences* 245 (2020). Ed. by C. Doglioni, D. Kim, G.A. Stewart, et al., p. 09013. DOI: [10.1051/epjconf/202024509013](https://doi.org/10.1051/epjconf/202024509013).
- [36] Marco Wiedmann, Maniraman Periyasamy, and Daniel D. Scherer. *Fourier Analysis of Variational Quantum Circuits for Supervised Learning*. Nov. 2024. DOI: [10.48550/arXiv.2411.03450](https://doi.org/10.48550/arXiv.2411.03450).

A Ansatzes

Fig. 6 shows the ansatzes used in this work. Specifically, we depict only a single variational layer and do not include the feature map.

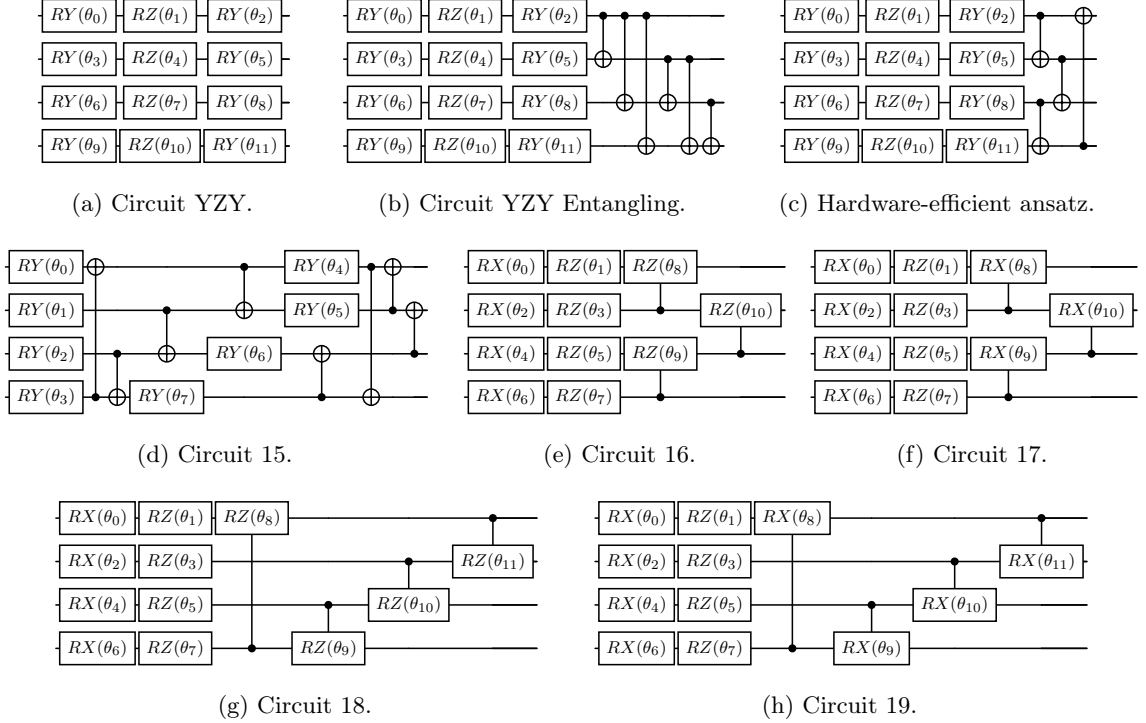


Fig. 6: The ansatzes used in this work, exemplarily for $n = 4$ qubits. Note the circular structure of the hardware-efficient ansatz (HEA).

B Effect of rotational axis on FCC

In Fig. 3a we utilize RY gates in the feature map of the models as we observed an absence of imaginary parts in *Circuit 15* for RX encoding gates. For the sake of completeness, we provide the Fourier fingerprints and comparison between the Fourier coefficient correlation (FCC) and expressibility in Fig. 7a and Fig. 7b respectively when the model is trained using RX encoding gates.

C Impact of the variance of coefficients in the FCC

The variance of the Fourier coefficients of quantum Fourier models (QFMs) is linked to the redundancy of the frequency, as observed in [20]. For the feature maps (FMs) studied in this work, this means that the variance of the coefficients decays exponentially towards higher frequencies. In this section, we consider whether this can lead to spurious correlations between coefficients which are independent but have the same redundancy. This is particularly important, since the variance of the coefficients enters in the denominator of our definition of correlation in equation Eq. 4. To numerically validate this, we randomly sample a set of coefficients from a Gaussian distribution with zero mean and the variance set to the degeneracy of the eigenvalues of the FM. Applying the Pearson method r we obtain the correlation between the coefficients samples, which are shown in Fig. 8 and can be seen to be all-zero, as expected.

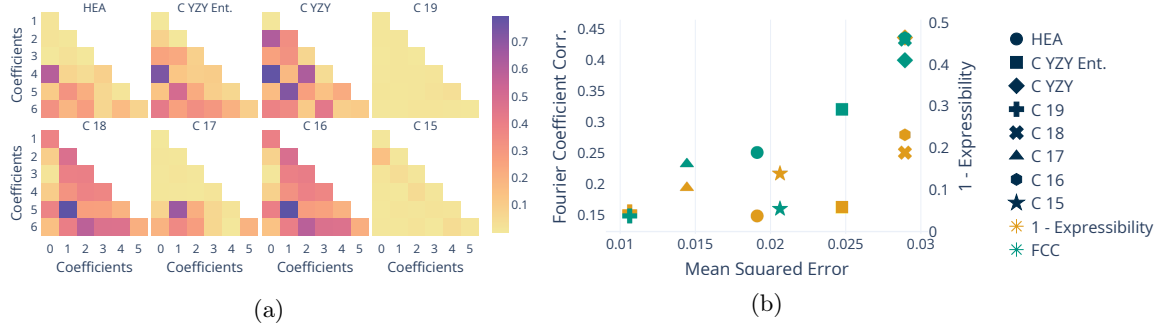


Fig. 7: Fourier fingerprints (a) and comparison between the FCC and expressibility complement over the mean squared error (MSE) for different ansatzes depicted by different shapes. Training on 1D Fourier series with 10 independent dataset seeds and 10 distinct parameter initializations. Features are encoded using RX gates.

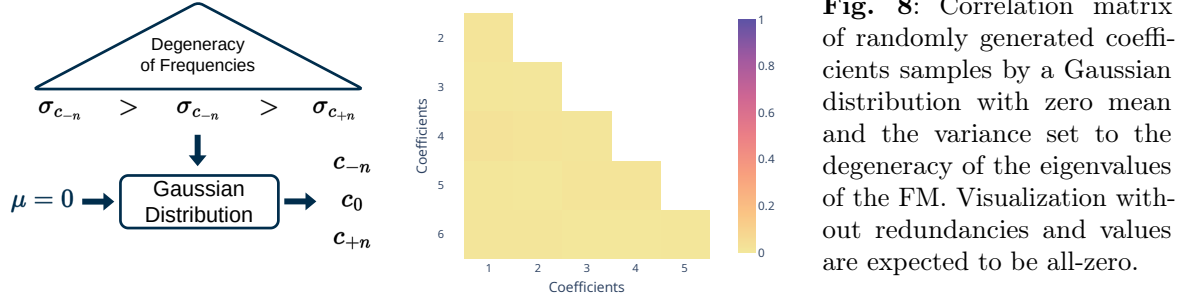


Fig. 8: Correlation matrix of randomly generated coefficients samples by a Gaussian distribution with zero mean and the variance set to the degeneracy of the eigenvalues of the FM. Visualization without redundancies and values are expected to be all-zero.

It is important that the FCC is independent of the variance of the coefficients, since, in practice, this varies in magnitude at different frequencies for different circuits. We can observe this effect in Fig. 9, where we show the real- and imaginary part of the variance decaying exponentially towards higher frequencies. The correlations are computed using $500 \cdot |\theta| \cdot 2^n \cdot D$ parameter samples with 10 different initial seeds on $n = 6$ qubit ansatzes. This finding is in line with a main statement from Ref. [20]. Here, specifically, we find that only *Circuit 15* and *Circuit 19* are exhibiting $\text{Var}(|c_\omega|) > 10^{-10}$ for all frequencies evaluated. Furthermore, we can see that *Circuit 15* does not exhibit an imaginary part when utilizing RX gates for the FM.

Notably, we observe that the mean value of the coefficients remains zero, *i.e.* that the absolute value of the coefficients is, independent of the frequency, zero-centered.

D Weighting the FCC

Considering the findings of App. C, the FCC as introduced in Eq. 5 does not take into account the degeneracy of the spectrum towards higher frequencies. To compensate for this, we perform additional experiments where a weighting strategy is applied to the fingerprints, giving higher frequencies a lower weight for correlations. Following this approach, we can restate the FCC as

$$\overline{\text{FCC}}_\Theta := \frac{1}{|\Omega|} \sum_{\omega, \omega' \in \Omega} |r_\Theta(\omega, \omega') w(\omega, \omega')| \quad (8)$$

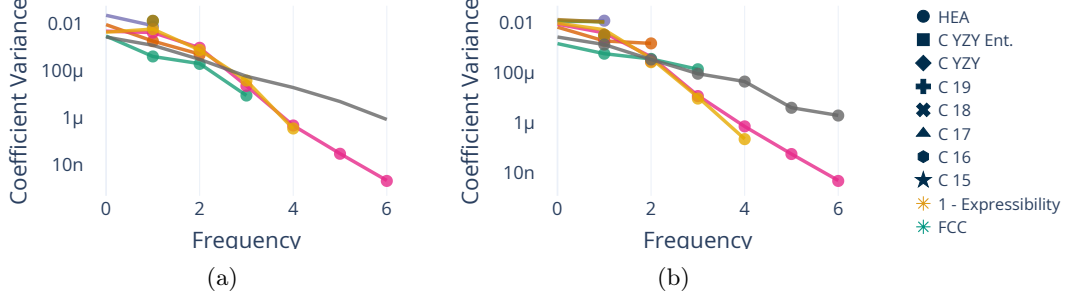


Fig. 9: Variances of the coefficient values $\text{Var}(\Re\{c_\omega\})$ (lines) and $\text{Var}(\Im\{c_\omega\})$ (markers) averaged over 10 different seeds for different frequencies ω and different ansatzes with (a) RX gates and (b) RY gates. Variances are cut off at 10^{-10} .

introducing the weighting function $w(\omega, \omega')$ which depends on the frequency pair. In the results depicted in Fig. 10 we applied a linear weighting $w(\omega, \omega') \sim (\omega + \omega')^{-1}$.

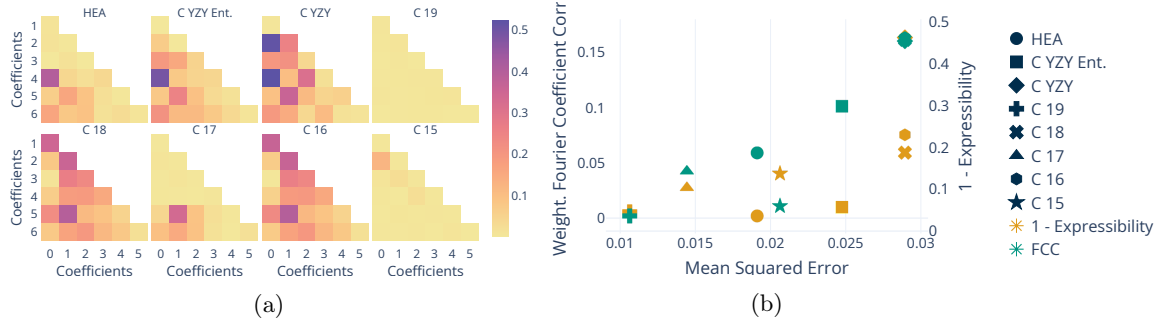


Fig. 10: Fourier fingerprints (a) and comparison between the FCC and expressibility complement over the mean squared error (MSE) for different ansatzes depicted by different shapes. Training on 1D Fourier series with 10 independent dataset seeds and 10 distinct parameter initializations. Features encoded using RX gates and linear weighting strategy on the FCC.

In Fig. 10a, we can observe that, due to the weighting, correlations between coefficients with a higher frequency index are being reduced when directly comparing to Fig. 7a. Furthermore, in Fig. 10b the FCC of *Circuit YZY* and *Circuit 17* adjusts slightly, such that the relation to the mean squared error (MSE) becomes more linear in general. Identical experiments with Pauli-RY encoding showed a less prominent effect and are therefore omitted in this section.

E Existence of coefficient correlations

While the existence of correlations between coefficient of the Fourier expansion of a QFM is visible from the numerical experiments we provide in this work, the work from Ref. [23, 36] provides the foundation for a more formal proof. Therefore we first restate a key finding from [36], *i.e.* the formula for the exact coefficients dependent on θ :

$$c_\omega(\theta) = \sum_{\substack{s, c \in \mathbb{N}_0^d \\ s', c' \in \mathbb{N}_0^w}} \frac{k_{s, c, s', c'} (-i)^{\sum_{j=1}^d s_j}}{2^{\sum_{j=1}^d (s_j + c_j)}} \times p_{s, c}(\omega) \prod_{k=1}^w \sin(\theta_k)^{s'_k} \cos(\theta_k)^{c'_k}. \quad (9)$$

Here $p(s, c, \omega)$ defines the sum of all coefficients belonging to ω , with s, c and s', c' counting the number of sine and cosine contributions by the input- and trainable parameters respectively. The constant $k_{s, c, s', c'}$ depends on the basis function following the notation in Ref. [36].

Proposition: Let $\theta \in [0, 2\pi)^w$ be fixed across ω . Then, even if $p(s, c, \omega)$ and $p(s, c, \omega')$ have disjoint supports, the functions $c_\omega(\theta)$ and $c_{\omega'}(\theta)$ can exhibit nonzero correlation due to their dependence on the shared basis functions $\left\{ \sin(\theta_k)^{s'_k} \cos(\theta_k)^{c'_k} \right\}$, *i.e.* if we consider a single parameter $\theta_k \in \theta$ per frequency ω , the correlations between different $c_\omega(\theta)$ already exist due to the right-hand side of Eq. 9.

The dependence on a shared basis function, however, does not imply that all ansatzes have equal distribution of correlations. Depending on the circuit, $p(s, c, \omega)$ can vary, resulting in a ansatz specific FCC. As already stated in Sec. 2.1, an ansatz with absolutely no correlation would be required to have an exponential number of parameters to account for the equally sized number of coefficients, rendering it untrainable in practice.

F Numerical Errors

Following the results of Fig. 3a, we provide a summary of the numerical errors in Tab. 1 as standard deviation $\sigma_m = \sqrt{\mathbb{E}[(\bar{m} - \mu(\bar{m}))^2]}$ of mean measurements \bar{m} (expressibility, FCC and MSE) for different ansatzes. Similarly, we provide the errors for the 2D Fourier series (*c.f.* Fig. 3b) and the high-energy physics (HEP) results (*c.f.* Fig. 5b) in Tab. 2 and Tab. 3 respectively. For all scenarios, we observe a low standard deviation consistent for all ansatzes and measurements.

σ	C 15	C 16	C 17	C 18	C 19	C YZY	C YZY Ent.	HEA
Expr.	3.6×10^{-3}	5.4×10^{-3}	3.8×10^{-3}	3.8×10^{-3}	1.4×10^{-3}	6.6×10^{-3}	1.8×10^{-3}	1.8×10^{-3}
FCC	9.6×10^{-4}	1.4×10^{-3}	1.6×10^{-3}	1.2×10^{-3}	9.3×10^{-4}	1.7×10^{-3}	1.2×10^{-3}	1.7×10^{-3}
MSE	1.0×10^{-3}	2.4×10^{-3}	6.6×10^{-5}	4.4×10^{-17}	1.5×10^{-3}	3.3×10^{-17}	2.4×10^{-3}	1.5×10^{-3}

Table 1: Standard deviation of mean measurements(expressibility, FCC and MSE) as depicted in Fig. 3a across all seeds for different ansatzes.

σ	C 15	C 16	C 17	C 18	C 19	C YZY	C YZY Ent.	HEA
Expr.	3.6×10^{-3}	5.4×10^{-3}	3.8×10^{-3}	3.7×10^{-3}	1.4×10^{-3}	7.6×10^{-3}	2.8×10^{-3}	1.8×10^{-3}
FCC	1.3×10^{-4}	2.9×10^{-4}	1.7×10^{-4}	2.4×10^{-4}	6.4×10^{-4}	2.5×10^{-4}	1.4×10^{-4}	1.6×10^{-4}
MSE	2.9×10^{-5}	0.0	2.2×10^{-5}	1.4×10^{-19}	3.5×10^{-5}	0.0	4.6×10^{-6}	2.0×10^{-5}

Table 2: Standard deviation of mean measurements(expressibility, FCC and MSE) as depicted in Fig. 3b across all seeds for different ansatzes.

σ	C 15	C 16	C 17	C 18	C 19	C YZY	C YZY Ent.	HEA
Expr.	3.6×10^{-3}	5.4×10^{-3}	3.8×10^{-3}	3.7×10^{-3}	1.4×10^{-3}	7.6×10^{-3}	2.8×10^{-3}	1.8×10^{-3}
FCC	1.3×10^{-4}	2.9×10^{-4}	1.7×10^{-4}	2.4×10^{-4}	6.4×10^{-4}	2.5×10^{-4}	1.4×10^{-4}	1.6×10^{-4}
MSE	2.9×10^{-5}	3.3×10^{-5}	3.0×10^{-5}	2.8×10^{-5}	2.4×10^{-5}	2.5×10^{-5}	3.0×10^{-5}	5.0×10^{-5}

Table 3: Standard deviation of mean measurements(expressibility, FCC and MSE) as depicted in Fig. 5b across all seeds for different ansatzes.

G Linking the FCC and the MSE

In this subsection, we derive how correlations between coefficients are reflected in the MSE. For the sake of simplicity, we only consider one-dimensional inputs such that $\mathbf{x} \mapsto x$ and $\boldsymbol{\omega} \mapsto \omega$, while $\boldsymbol{\theta}$

remains a vector of parameters. Consider the target Fourier series $\hat{f}(x) = \sum_{\omega \in \Omega} \hat{c}_\omega \exp^{i\omega x}$ and the truncated Fourier series of the model $f(x, \boldsymbol{\theta}) = \sum_{\omega \in \Omega} c_\omega(\boldsymbol{\theta}) \exp^{i\omega x}$. We now want to minimize a dataset sampled from $x \in \mathcal{X}$ using the MSE

$$\begin{aligned} \mathcal{L}(x, \boldsymbol{\theta}) &= \frac{1}{|\mathcal{X}|} \int_{x \in \mathcal{X}} |f(x, \boldsymbol{\theta}) - \hat{f}(x)|^2 dx \\ &= \frac{1}{|\mathcal{X}|} \int_{x \in \mathcal{X}} \left| \sum_{\omega \in \Omega} (c_\omega(\boldsymbol{\theta}) - \hat{c}_\omega) \exp^{i\omega x} \right|^2 dx \\ &\stackrel{(1)}{=} \sum_{\omega \in \Omega} |c_\omega(\boldsymbol{\theta}) - \hat{c}_\omega|^2 \end{aligned} \tag{10}$$

where in (1) we assume the input interval $\mathcal{X} = [0, 2\pi)$ such that $\exp^{i\omega x}$ is orthonormal over \mathcal{X} and apply Parseval's identity to simplify. It should be noted that we assume the frequencies in the target function are equal to those of the QFM, which is not the case in general but suffices for the study in this work.

As we want to argue about an arbitrary $\boldsymbol{\theta} \in \Theta$, but \mathcal{L} depends on a specific realization of $\boldsymbol{\theta}$, we must rewrite a statistical form of the loss $\mathbb{E}_\Theta[\mathcal{L}(\boldsymbol{\theta})]$ based on [Eq. 10](#) as

$$\begin{aligned} \mathcal{L}(\boldsymbol{\theta}) &= \sum_{\omega} (|c_\omega(\boldsymbol{\theta})|^2 + |\hat{c}_\omega|^2 - 2\Re(c_\omega^*(\boldsymbol{\theta})\hat{c}_\omega)) \\ \mathbb{E}_\Theta[\mathcal{L}(\boldsymbol{\theta})] &\stackrel{(1)}{=} \sum_{\omega \in \Omega} \left[\mathbb{E}_\Theta |c_\omega(\boldsymbol{\theta})|^2 + |\hat{c}_\omega|^2 - 2\Re(\mathbb{E}_\Theta [c_\omega(\boldsymbol{\theta})] \hat{c}_\omega^*) \right] \\ &\stackrel{(2)}{=} \sum_{\omega \in \Omega} \left[\mathbb{E}_\Theta |c_\omega(\boldsymbol{\theta})|^2 + |\hat{c}_\omega|^2 \right] \\ &\stackrel{(3)}{=} \sum_{\omega \in \Omega} \left[\sigma_\Theta^2(c_\omega(\boldsymbol{\theta})) + |\hat{c}_\omega|^2 \right] \end{aligned} \tag{11}$$

where in (1) we convert to a statistical loss with $\boldsymbol{\theta} \in \Theta$ and in (2) we assume zero mean based on [App. C](#), *i.e.* $\mathbb{E}_\Theta [c_\omega(\boldsymbol{\theta})] = 0$ such that $\Re(\mathbb{E}_\Theta [c_\omega(\boldsymbol{\theta})] \hat{c}_\omega^*) = 0$ with $(\cdot)^*$ denoting the complex conjugate and $\Re(\cdot)$ the real part of a complex number.

Notably, \mathcal{L} is separable in ω , therefore the final statement in [Eq. 11](#) only captures the standard deviation of each coefficient individually, corresponding to the diagonal of the covariance matrix K . The correlation in the off-diagonal elements, however, puts additional constraints on the optimizer, as individual coefficients can't be adjusted individually. We can capture this in \mathcal{L} as well, by assuming that each coefficient is actually not dependent on a single frequency, but on all other frequencies in Ω instead, as discussed in [App. E](#). This can be accounted for by substituting $c_\omega(\boldsymbol{\theta}) = \sum_{\omega' \in \Omega} \zeta(\omega, \omega'; \boldsymbol{\theta})$, where $\zeta(\omega, \omega'; \boldsymbol{\theta})$ is a proxy coefficient, that shares contributions to ω and ω' given the parameter vector $\boldsymbol{\theta}$. The proxy coefficient for $\omega = \omega'$ would then reflect the prior assumption of a fully separable loss, still allowing for a scenario where the coefficients are fully independent, *i.e.* where $\zeta(\omega, \omega'; \boldsymbol{\theta}) = 0 \forall \omega \neq \omega'$ such that $c_\omega(\boldsymbol{\theta}) = \zeta(\omega, \omega; \boldsymbol{\theta})$.

Given this assumption, we restate the second last equation [Eq. 11](#) as follows:

$$\begin{aligned}
\mathbb{E}_\Theta[\mathcal{L}(\boldsymbol{\theta})] &= \sum_{\omega \in \Omega} \left[\mathbb{E}_\Theta \left[\left| \sum_{\omega' \in \Omega} \zeta(\omega, \omega'; \boldsymbol{\theta}) \right|^2 + |\hat{c}_\omega|^2 \right] \right. \\
&\stackrel{(1)}{=} \sum_{\omega \in \Omega} \left[\sum_{\omega', \omega'' \in \Omega} [\mathbb{E}_\Theta [\zeta(\omega, \omega'; \boldsymbol{\theta}) \zeta^*(\omega, \omega''; \boldsymbol{\theta})]] + |\hat{c}_\omega|^2 \right] \\
&\stackrel{(2)}{=} \sum_{\omega \in \Omega} \left[\sum_{\omega', \omega'' \in \Omega} r_\Theta(c_{\omega'}, c_{\omega''}) \sigma_\Theta(c_{\omega'}) \sigma_\Theta(c_{\omega''}) + |\hat{c}_\omega|^2 \right]
\end{aligned} \tag{12}$$

where in (1) we expanded the complex inner product that requires introducing two additional dummy frequencies ω' and ω'' , which can be regarded as directional interactions between frequencies.

From [Eq. 4](#) we restate the Pearson correlation between coefficients of frequency ω and ω' in a slightly different form as

$$r_\Theta(c_\omega, c_{\omega'}) = \frac{K_\Theta(c_\omega, c_{\omega'})}{\sqrt{\sigma_\Theta^2(c_\omega) \sigma_\Theta^2(c_{\omega'})}} \stackrel{\bar{c}=0}{=} \frac{\mathbb{E}_\Theta |c_\omega(\boldsymbol{\theta}) c_{\omega'}(\boldsymbol{\theta})|}{\sigma_\Theta(c_\omega) \sigma_\Theta(c_{\omega'})} \tag{13}$$

with $\mathbb{E}_\Theta(\cdot)$ being the expectation value of (\cdot) over Θ , $\sigma_\Theta^2(c_\omega) = \text{Var}_\Theta(c_\omega) = \mathbb{E}_\Theta |c_\omega(\boldsymbol{\theta}) c_{\omega'}(\boldsymbol{\theta})|$ being the standard deviation of c_ω , $K_\Theta(c_\omega, c_{\omega'})$ the covariance between c_ω and $c_{\omega'}$ and \bar{c}_ω the mean over Θ . Using the right-hand side of [Eq. 13](#) we can substitute the inner term in (2), which introduces the Pearson correlation to the overall loss function.

As stated in [Eq. 12](#), the FCC is the sum of over all frequency pairs of r and therefore linearly related. Therefore, the FCC is also closely related to \mathcal{L} but strongly weighted by the variances of the coefficients. Following the weighting strategy introduced in [App. D](#), we can set $w(\omega', \omega'') = \sigma_\Theta(c_{\omega'}) \sigma_\Theta(c_{\omega''})$ and therefore forcefully restating the final loss equation as follows:

$$\begin{aligned}
\mathbb{E}_\Theta[\mathcal{L}(\boldsymbol{\theta})] &= \sum_{\omega \in \Omega} \left[\sum_{\omega', \omega'' \in \Omega} r_\Theta(c_{\omega'}, c_{\omega''}) w(\omega', \omega'') + |\hat{c}_\omega|^2 \right] \\
&= \sum_{\omega \in \Omega} \left[\overline{\text{FCC}}_\Theta |\boldsymbol{\Omega}|^{-1} + |\hat{c}_\omega|^2 \right] \\
&= \overline{\text{FCC}}_\Theta \sum_{\omega \in \Omega} |\hat{c}_\omega|^2.
\end{aligned} \tag{14}$$

Here, only the FCC and the contribution of the squared absolute value of each target coefficient remain. The findings from Ref. [\[20\]](#) suggest an exponential decay of the variance towards high frequency components, providing a practical hint on estimating σ_Θ . This equation analytically summarizes our main contribution of this work; the loss of learning a QFM on a Fourier series with the same number of frequencies is linearly dependent on the (weighted) FCC, *i.e.* the correlation between the frequency components of the QFM.

H Computing the expressibility & complexity estimate

The expressibility is a commonly used metric that quantifies how a given ansatz can cover the Hilbert space spanned by a parameterized quantum circuit (PQC). It can be calculated using the KL-divergence [\[17\]](#) between the model $\int_{\boldsymbol{\theta}} (|\psi_{\boldsymbol{\theta}}\rangle \langle \psi_{\boldsymbol{\theta}}|)^{\otimes t} d\boldsymbol{\theta}$ and the distribution of the Haar-integral

$\int_{\text{Haar}} (|\psi\rangle\langle\psi|)^{\otimes t} d\psi$ of a state t -design with $D_{\text{KL}}\left(\hat{P}_{\text{Model}}(F; \theta) \| P_{\text{Haar}}(F)\right)$. Here $F = |\langle\psi_{\phi} | \psi_{\phi}\rangle|^2$ describes the fidelity between two states.

Generally speaking, an ansatz with a high expressibility is expected to have a high chance of reaching an arbitrary state, as parameters are likely to be sampled in the desired area of the Hilbert space. For this reason, the expressibility can be used as a metric to estimate the performance of a given ansatz. However, it should also be noted that ansatzes with high expressibility are also more prone to the Barren Plateau phenomenon as described in Ref. [26].

Calculating the expressibility is a computationally expensive task as it requires simulation of the density matrix. While the distribution of the Haar integral can be cached, the distribution of the model requires sampling the parameters and therefore varies with the number of layers. Therefore, the overall complexity is at $\mathcal{O}(MN^3)$ (matrix-matrix multiplication) where M is the number of parameter samples used to calculate the expressibility and $N = 2^n$ is the dimensionality of the Hilbert space spanned by n qubits. Furthermore, the expressibility can only be calculated in simulation, as access to the density matrix is naturally not available on real hardware.

In comparison, the FCC metric only requires computing the expectation value (matrix-vector multiplication) but adds the overhead of the fast Fourier transform (FFT) $\mathcal{O}(K \log(K))$ where K is the number of input samples, resulting in a complexity of the FCC being $\mathcal{O}(MN^2 K \log(K))$. To prevent aliasing, K has to be $\geq 2 \max(\Omega)$, where $\max(\Omega)$ is the highest frequency of the QFM. For the case of a D -dimensional input, the number of samples required is $K \geq (2 \max(\Omega))^D$. Therefore, the overall complexity for computing the FCC of a n -qubit QFM with D -dimensional input and the highest available frequency $\max(\Omega)$ becomes $\mathcal{O}(MN^2 (\max(\Omega))^D \log(\max(\Omega)))$, when just satisfying the sampling theorem. Considering a window length K being power of 2, the complexity of the FFT can further be reduced according to Ref. [6] to $K/2 \log_2(K)$ which, however, does not reduce the overall complexity in the asymptotic limit.

In case of having just a single-layered QFM, where the highest frequency is just n [28], it allows us to simplify the expression to $\mathcal{O}(MN^2 n^D \log_2(n))$. In a scenario where the number of qubits is equal to the number of layers, we find that $\max(\Omega) = n^2$ and the FCC complexity becomes $\mathcal{O}(MN^2 n^{2D} \log_2(n))$ which is still easier to compute than the expressibility. The worst case (and unlikely) scenario would be a single qubit QFM with n layers, where the (theoretically) highest frequency is still n , but $N = 2$ and therefore the computational complexity of the expressibility would reduce to $\mathcal{O}(M)$, while the FCC is $\mathcal{O}(Mn^D \log_2(n))$. To summarize, a comparison with the expressibility complexity $\mathcal{O}(M2^{3n})$ shows that in the limit of n , the FCC with $\mathcal{O}(MN^2 (\max(\Omega))^D \log(\max(\Omega)))$ is easier to compute, regardless of D and any (feasible) constraint on the number of layers.

Furthermore, the FCC metric is also more suitable for real hardware as the expectation value can be directly calculated on the device. In contrast, the expressibility requires full-state tomography which is exponentially costly in the number of qubits, whereas the FCC requires only a single measurement basis. The error introduced by shot noise is $1/\sqrt{N_{\text{shots}}}$ with N_{shots} being the number of shots taken and applicable to both measures.

I High-Energy Physics

Additional numerical results

In the following, we provide additional numerical results for training on the HEP dataset where the setup is identical to Sec. 3.2 but, instead of the MSE, compare the Kullback-Leibler (KL) divergence and Huber loss to the FCC and expressibility. The result of this comparison can be seen in Fig. 11a and Fig. 11b respectively.

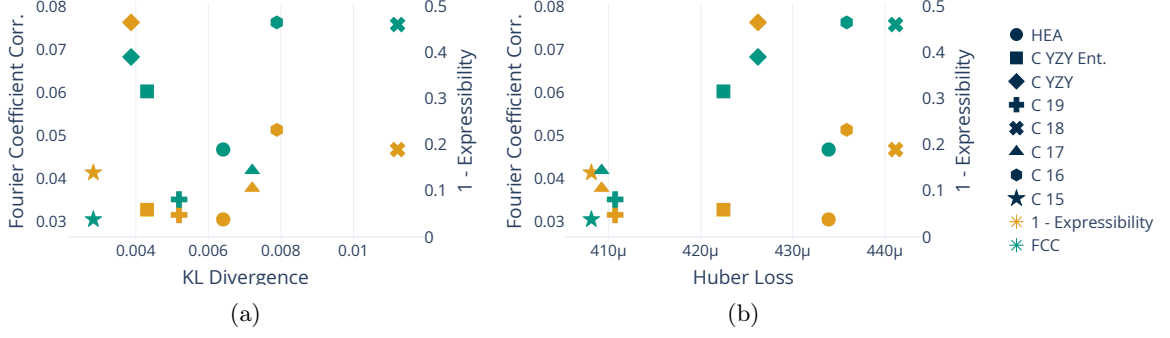


Fig. 11: Comparison of FCC and expressibility complement over the KL divergence (a) and Huber loss (b) for different ansatzes (color coded). Training on 2D HEP dataset with averaged over 10 independent dataset seeds and 10 distinct parameter initializations.

For the KL-divergence, the FCC and expressibility both fail as predictors, although *Circuit 15* and *Circuit 18* still represent the best and worst performing circuits, as already seen in Fig. 5. In contrast, the results for the Huber loss are almost identical with the results for the MSE as shown in Fig. 5.

Physical foundations

Next, we want to provide an explanation on the physical foundations of the HEP dataset used in this work. In high-energy proton–proton collisions at the Large Hadron Collider (LHC), the dominant processes involve interactions between constituent partons; quarks and gluons. These quark–gluon scatterings lead to the production of jets, collimated sprays of hadrons that are experimentally observed as signatures of the underlying partonic activity.

At leading order (LO), quark–gluon scattering produces two outgoing partons that hadronize into two jets, corresponding to the final-state quark and gluon, see Fig. 12 left. The corresponding Feynman diagram features a single gluon exchange vertex.

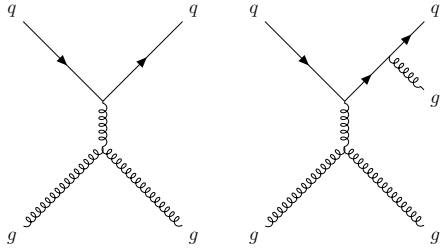


Fig. 12: Quark–gluon scattering at LO and next-to-leading order (NLO). The additional gluon emission in NLO corresponds to an extra vertex with a factor of the strong coupling constant α_s , reducing the interaction probability and increasing the number of jets observed.

Beyond LO, at NLO and higher, additional gluon emissions occur, see Fig. 12 right. Each emission corresponds to an extra vertex in the Feynman diagrams, contributing a factor of the strong coupling constant α_s , which quantifies the interaction strength of quantum chromodynamics (QCD). Since α_s runs with the energy scale, it decreases logarithmically at higher momentum transfers (asymptotic freedom). This running controls the probability of multiple gluon emissions and thus the jet multiplicity.

The presence of three or more jets arises naturally from these additional gluon emissions during the parton shower phase, reflecting the increased complexity of the event. The number of jets and their momentum distribution provide direct insight into the QCD dynamics and the value of α_s at the relevant scale.

The center-of-mass energy E_{cm} plays a central role because it sets the scale for the hard scattering process. Higher E_{cm} implies access to larger momentum transfers, reducing α_s and opening greater phase space for gluon radiation. Consequently, at LHC energies, this results in higher jet multiplicities and broader momentum spectra, making E_{cm} a fundamental metric for studying jet formation and modeling QCD interactions.

J Sampling

Shot noise

Considering the expectation value of a QFM $f(\mathbf{x}, \boldsymbol{\theta}) = \langle 0 |^{\otimes n} U^\dagger(\mathbf{x}, \boldsymbol{\theta}) \mathcal{M} U(\mathbf{x}, \boldsymbol{\theta}) | 0 \rangle^{\otimes n}$, it is commonly known that the true error due to a finite number of S shots is given by $1/\sqrt{S}$. Therefore, we can state \tilde{f} , which is the expectation value f with some shot noise $\delta(\mathbf{x})$.

$$\tilde{f}(\mathbf{x}, \boldsymbol{\theta}) = f(\mathbf{x}, \boldsymbol{\theta}) + \delta(\mathbf{x}) \quad \text{with} \quad |\delta(\mathbf{x})| \leq \frac{1}{\sqrt{S}} \quad \forall \mathbf{x} \quad (15)$$

Due to the linearity of the FFT and $\Delta c_\omega = \tilde{c}_\omega - c_\omega$ being the deviation in the Fourier coefficients caused by shot noise and we can say that $\Delta c_\omega = \sum_{\mathbf{x}} \delta(\mathbf{x}) \exp(i\omega\mathbf{x})$. With $\delta(\mathbf{x}) \leq \frac{1}{\sqrt{S}}$, we have that

$$|\Delta c_\omega| \leq \sum_{\mathbf{x}} |\delta(\mathbf{x})| \cdot |e^{i\omega\mathbf{x}}| = \sum_{\mathbf{x}} |\delta(\mathbf{x})| \leq \frac{1}{\sqrt{S}} |\mathcal{X}|. \quad (16)$$

Because for a single FFT, we require $|\mathcal{X}|$ sampling points, the error for a single frequency coefficient accumulates linearly while the number of shots reduces this error by $\frac{1}{\sqrt{S}}$.

Sampling error

The Pearson correlation method requires statistical information of $c_\omega(\boldsymbol{\theta})$ over Θ . For any practical scenario, the actual number of samples M drawn from Θ is therefore important to consider. We assume that $c_\omega(\boldsymbol{\theta})$ is zero-centred (*c.f.* App. C) and because $f \in [-1, 1]$, the energy of the Fourier transform is bounded, requiring the coefficients to be bounded as well. The standard error for r given a finite sample size M is given by [2]

$$\sigma_{r_{\omega, \omega'}} \approx \sqrt{\frac{1 - r_{\omega, \omega'}^2}{(M - 1)^2}}, \quad (17)$$

where $\sigma_{r_{\omega, \omega'}}$ denotes the deviation from the true Pearson correlation r that converges to 0 in the limit of $M \rightarrow \infty$. As the FCC is just the summation of $r_{\omega, \omega'}$ over all frequency pairs, we can estimate a similar error as

$$\sigma_{FCC} \approx \frac{1}{|\Omega|} \sum_{\omega, \omega'} \sqrt{\frac{1 - r_{\omega, \omega'}^2}{(M - 1)^2}} \stackrel{(1)}{=} \frac{\sqrt{1 - \bar{r}^2}}{|\Omega|(M - 1)} \quad (18)$$

where, in (1), we assume independence of the correlation estimates across frequency pairs, *i.e.* all correlations have a similar variance. Therefore, we can utilize the average correlation \bar{r} of a QFM and the error in the FCC scales as $\sim \frac{1}{M}$ with the number of samples M .

Variances of coefficients

Practically, we already know that the variance of c_ω decays exponentially with the frequency (*c.f.* App. C), which we can model by $\sigma_\Theta^2(c_\omega) \sim \beta e^{-\alpha \|\omega\|}$ with $\beta > 0$ and $\alpha > 0$ being some constants depending on the specific FM and ansatz. Because of this exponential decay in the denominator of $r_{\omega, \omega'}$, σ_{FCC} is dominated by the sampling variability for higher frequencies. We can roughly estimate

this by $\sigma_{FCC} \approx \frac{1}{M} e^{\alpha(\|\omega\| + \|\omega'\|)}$. This result implies an exponential requirement on M already, if high frequency accuracy is required. However, if we consider that redundancies decay towards higher frequencies as well [20], we can expect fewer parameters contributing to high-frequent c_ω , which even increases the requirement on the number of parameter samples M .

Number of qubits

By now, we considered a fixed number of qubits, and therefore also a fixed length of the parameter vector $|\theta|$ (given a particular ansatz). Changing the number of qubits naturally changes the number of parameters and, therefore, the requirement on M . However, because the Hilbert space increases with 2^n , the question arises whether there is an even stronger requirement on M than just compensating for the higher number of parameters. To show that M does not have to scale exponentially with n , we consider an average expectation value \bar{f} as

$$\bar{f}(\mathbf{x}) = \frac{1}{M} \sum_{\theta \in \Theta} f(\mathbf{x}, \theta) \quad \text{with} \quad |\theta| = M. \quad (19)$$

Because the expectation value is bounded in $[-1, 1]$, \bar{f} must be bounded as well, and we can apply Hoeffding's inequality

$$\mathbb{P} \left(\left| \hat{\bar{f}} - \bar{f} \right| \geq \epsilon \right) \leq 2 \exp(-2M\epsilon^2) \quad (20)$$

which allows us to estimate the probability that an average $\hat{\bar{f}}$ deviates from the true \bar{f} by less than ϵ .